Research Square

Preprints are preliminary reports that have not undergone peer review.
They should not be considered conclusive, used to inform clinical practice,
or referenced by the media as validated information.

# Epitope-resolved evaluation of RFdiffusion for de novo binder design across the EGFR extracellular domain

**Shiqi Zhuang**
Guangdong University of Technology
**Wanqin Zhang**
Chinese University of Hong Kong, Shenzhen
**Geshu Zhang**
Chinese University of Hong Kong, Shenzhen
**Zihan Chen**
Guangdong University of Technology
**Bohan Chen**
Guangdong University of Technology
**Yuheng Mei**
Chinese University of Hong Kong, Shenzhen
**Jingchuan Xue**
Guangdong University of Technology
**Hongli Hu**
Chinese University of Hong Kong, Shenzhen
**Haizhan Jiao**
jiaohaizhan@cuhk.edu.cn
Chinese University of Hong Kong, Shenzhen

**Article**

**Keywords:** EGFR, extracellular domain, de novo binder design, RFdiffusion, ProteinMPNN, AlphaFold2

**Posted Date:** November 25th, 2026

**DOI:** https://doi.org/10.21203/rs.3.rs-11712832/v1

**License:** This work is licensed under a Creative Commons Attribution 4.0 International License. Read Full License

**Additional Declarations:** No competing interests reported.

## Abstract

Which surface of a protein target should a de novo binder campaign aim at? We addressed this question for the epidermal growth factor receptor (EGFR) by running one standard pipeline — RFdiffusion for backbones, ProteinMPNN for sequences, AlphaFold2 for filtering — on eleven structures of the extracellular domain, each in complex with a different antagonist. The contact residues of each antagonist defined the hotspot residues, so that every campaign targeted an epitope already known to be accessible. Of 330,000 designs, 12,547 passed the computational filters. The seven inputs with hotspots on subdomain III supplied 12,486 of these; a DI input returned 52 designs, a DIII–linker input nine, and the DII/DIII and EGFRvIII-derived DIV inputs returned none. Yield varied twentyfold even between two DIII inputs, and hotspot number did not explain the difference: what mattered was the epitope, not the subdomain label. Binder length also mattered, with 50–59 residues performing best. Eleven DIII-directed designs were expressed and tested by surface plasmon resonance; all eleven bound, with apparent affinities of 0.54–11.5 μM, yet AlphaFold3 confidence did not predict binding strength. Epitope choice, rather than subdomain identity, dominates the outcome of a de novo binder campaign.

## Introduction

The epidermal growth factor receptor (EGFR) is a receptor tyrosine kinase at the plasma membrane that controls proliferation, differentiation and survival[1, 2]. It is overexpressed, amplified or mutated in a large fraction of non-small cell lung cancers, colorectal cancers and glioblastomas, which is why it has been pursued so intensively as a drug target[3, 4]. Its extracellular region is organised into four subdomains, DI to DIV, that together bind ligand and drive receptor dimerisation[1, 2]. Antibodies against defined epitopes of this region are already in clinical use, with cetuximab and panitumumab as the best-known examples[5, 6]. Smaller scaffolds have been developed as alternatives to whole antibodies, mainly for better tissue penetration and lower manufacturing cost[7–9]. Building such a binder against a chosen epitope, however, has until recently required extensive experimental screening and repeated rounds of optimisation[7–10].

Deep learning has changed what is practical in binder design[11–14]. RFdiffusion, which grew out of RoseTTAFold, generates backbones by denoising from random noise, conditioned on a target surface and a set of hotspot residues; the scaffolds it returns differ in topology but are all compatible with the requested interface[12]. ProteinMPNN then assigns sequences to those backbones by inverse folding, and AlphaFold2 (AF2) scores the resulting complexes, which allows very large libraries to be screened computationally before any experiment[15, 16]. Pipelines built on the same principles have reported experimental success rates of 10–100%, depending on the target[13, 17–19].

EGFR has already served as a test case, and earlier work has set a high standard. Cao et al. designed binders from the target structure alone and reached nanomolar affinities for several targets, EGFR among them; one of their EGFR binders was later used as the antigen-binding domain of a chimeric antigen receptor that outperformed an scFv-based receptor in glioblastoma models[10, 20]. A community competition on the same receptor collected more than 1,800 designs, of which 601 were expressed and measured. The best reached 82 nM, and the organisers concluded that the computational metrics then in use ranked designs poorly against experiment[21]. What is missing is a controlled comparison in which one pipeline and one set of filters are applied to epitopes from different subdomains of the same receptor, with designs from one subdomain carried on to experiment. That is what we report here.

We chose eleven structures of the EGFR ectodomain, each in complex with an antibody, nanobody, repebody or adnectin. In every case the residues that contact the bound antagonist became the hotspots, so that every campaign was aimed at an epitope already known to be accessible; differences in outcome between inputs therefore reflect how readily each surface can be designed against, not whether it can be bound at all. Six thousand backbones and 30,000 sequences were generated per input and filtered with AF2. We then asked how the epitope targeted, binder length and one cycle of

FastRelax affected the fraction of designs passing, and we expressed and measured eleven DIII-directed designs by surface plasmon resonance (SPR).

## Results

***Eleven epitope-defined inputs across the EGFR ectodomain***

Eleven structures of the EGFR ectodomain, each with a bound protein antagonist, served as inputs (Fig. 1a). The bound antagonist defines the interface. Every EGFR residue in contact with it was identified with the *interfaces* tool in ChimeraX and taken as a hotspot, so each campaign was aimed at an epitope that some natural or engineered binding protein is already known to engage. The EGFR chain was then cropped to the segment listed for each structure in Fig. 1a — from 191 residues (3C09) to 405 residues (4KRP), numbering as in the deposited construct.

Hotspots were distributed as follows (Fig. 1b). Seven structures placed them entirely on DIII: 3B2U (Fab IMC-11F8[22]), 5SX5 (panitumumab[6]), 3C09 (matuzumab[23]), 3P0Y (Fab DL11[24]), 4UV7 (Fab GC1118A[25]), 5XWD (059-152-Fv[26]) and 4KRM (nanobody 7D12[27]). 4KRP (nanobody 9G8) carried hotspots on DII and DIII together, so it presents a composite surface rather than an isolated DII patch[27]. 4UIP (repebody rAC1) had 20 hotspots, most on DIII and the rest in the DIII–DIV linker[28]. 3QWQ (adnectin) is the only input with hotspots on DI[29], and 8UKV (nanobody 34E5) the only one on DIV[30].

Each input was run in six jobs, for binder lengths of 40–49, 50–59, 60–69, 70–79, 80–89 and 90–99 residues, with 1,000 backbones per job. We used the Complex_beta_ckpt weights rather than the default model. The default RFdiffusion checkpoints are heavily enriched in α-helical folds, and the β-sheet-biased checkpoint widens the range of topologies that the designs start from[12]. ProteinMPNN assigned four sequences per backbone without relaxation and one after a single FastRelax cycle[15,31], giving 6,000 backbones and 30,000 sequences per input, and 66,000 backbones and 330,000 sequences in total. All designs were scored with the AF2 initial-guess protocol of dl_binder_design[10], so the order was backbone generation, sequence design with or without FastRelax, and AF2 prediction. Sequences and scores for every design are provided as Supplementary Information.

***Computational design outcomes vary across epitopes***

PAE_interaction, the predicted aligned error averaged over interchain residue pairs, was our primary measure of interface confidence; lower values mean a more confident relative placement of the two chains. Across the 330,000 designs it ranged from 3.666 to 28.975 Å, and about 87% of designs fell between 20 and 30. An error of 20–30 Å in the position of the partner chain is large, so for most designs the predicted interface carried very little confidence. The inputs nonetheless separated. For 3B2U, 5SX5, 3C09, 3P0Y, 4UV7, 5XWD and 4KRM a sizeable fraction of designs sat well below the main cluster, reaching values of 10 and sometimes below 5. For 4UIP and 3QWQ only a small fraction fell below 10, and for 4KRP and 8UKV none did (Fig. 2a).

Designs were kept when PAE_interaction was below 10, binder pLDDT above 80, and binder RMSD below 1 Å — the thresholds recommended for dl_binder_design[10]. Here pLDDT refers to the binder chain alone, RMSD is calculated on binder Cα atoms after superposing the AF2 model onto the design model, and PAE_interaction is averaged over the interchain residue pairs of the predicted interface. Of the 330,000 designs, 12,547 (3.8%) passed. Counts and rates varied widely across targets (Fig. 2b): 3B2U 1,858 (6.2%), 5SX5 2,174 (7.2%), 3P0Y 1,520 (5.1%), 4UV7 3,174 (10.6%), 5XWD 1,675 (5.6%), 4KRM 1,928 (6.4%) and 3C09 157 (0.5%). The remaining four inputs fared far worse. No design passed for 4KRP, whose hotspots span a composite DII/DIII surface, or for 8UKV, the EGFRvIII-derived DIV construct; the DIII–linker input 4UIP yielded only nine passing designs (0.03%), and the DI input 3QWQ yielded 52 (0.17%). A zero count

means only that none of the 30,000 designs for that input met these deliberately stringent filters; it does not show that the surface cannot be designed against.

Among passing designs, the PAE_interaction distributions separated the strong inputs from the weak ones (Fig. 2c). For the seven DIII-only inputs, medians fell within a narrow band (7.020–7.333), and the best designs reached PAE_interaction values down to 3.666 Å. For 4UIP and 3QWQ, no passing design scored below 5, with medians of 9.663 and 8.834. Taken together, the eleven inputs indicate that designs targeted at the DIII core passed the computational filters most often and with the best scores, whereas inputs whose hotspots extended beyond it — to DI, the DII/DIII boundary, the DIII–DIV linker, or DIV — passed rarely or not at all.

The seven DIII-only inputs were far from equivalent. 4UV7 returned 3,174 passing designs (10.6%) and 3C09 only 157 (0.5%), a twentyfold difference within one domain. The two hotspot sets are similar in size, nine residues in 4UV7 and eleven in 3C09, but they sit on different parts of the surface. The 4UV7 set lies between residues 325 and 362, in the N-terminal part of DIII, whereas the 3C09 set lies between 449 and 466, close to the DIII–DIV junction. The difference between 4UV7 and 3C09 more likely lies in the shape and continuity of the surface the hotspots define.

***Binder length and FastRelax***

Passing designs were grouped by length class. Each class started from the same number of sequences (55,000), so counts and rates carry the same information. The 50–59 class gave the highest rate (2,648 of 55,000, 4.8%), followed by 60–69 (2,449, 4.5%) and 40–49 (2,421, 4.4%); the rate then fell to 3.8% (70–79, 2,111), 3.1% (80–89, 1,680) and 2.3% (90–99, 1,238). The trend was not uniform. The 50–59 class was the most productive for five of the seven DIII-only inputs (3B2U, 5SX5, 3P0Y, 4UV7 and 5XWD), but 40–49 was best for 4KRM and 3C09, and also for the DI input 3QWQ (Supplementary Fig. S1). In aggregate, designs of 40–69 aa produced 60% of all passing designs (7,518 of 12,547) and the pass rate fell to half its peak in the 90–99 class, but the exceptions above show this pooled preference for intermediate length is target-dependent rather than a rule.

One cycle of FastRelax raised the yield slightly. Of 66,000 relaxed sequences, 2,942 (4.46%) passed; of 264,000 unrelaxed sequences, 9,605 (3.64%) did. That is 0.82 percentage points, or a relative increase of 22.5%, and the direction was the same in all nine inputs that produced any passing design (Supplementary Fig. S2). The effect on the score itself was marginal. Median PAE_interaction among passing designs was 6.955 with FastRelax and 7.154 without, a difference of 0.199 Å, and the two distributions almost completely overlapped (Fig. 2e). For most targets, the median PAE_interaction of passing designs was lower with one cycle of FastRelax than without it; for 3P0Y it was essentially unchanged. The only target where the median was higher was 3C09, at 7.792 with FastRelax versus 7.067 without (Supplementary Fig. S2). The comparison is between sequences rather than backbones, since each backbone contributed one relaxed and four untreated sequences. What the data support is the narrower claim that omitting FastRelax costs little in yield, so the step is helpful but not essential; this is consistent with the RFdiffusion authors' observation that the FastRelax step did not produce large improvements in *in silico* success rates for binder design[12].

***Expression, purification and surface plasmon resonance***

Candidates for experimental testing were drawn from the 12,547 passing designs. The 804 designs from this set with PAE_interaction below 5 were submitted to the AlphaFold3 server, and those with an ipTM of 0.9 or higher were kept for manual inspection. We excluded designs whose poorly packed cores might compromise expression, took scaffold diversity into account, and selected eleven binders for expression (Binders 1–11; Table 1). In AF3 re-predictions, all eleven scored an ipTM of 0.90–0.94 and a pTM of 0.72–0.75 (Fig. 3). The eleven binders derive from six of the seven DIII-only inputs and are 70–98 residues long; notably, none belongs to the 50–59 residue class, the most productive in the screen. This gap reflects our manual selection rather than the screen itself: in the shorter passing designs, the

predicted models often showed thin, poorly packed cores, and these binders were judged less likely to fold stably, so we favoured longer designs with more extensive core packing.

The binders were expressed in *E. coli* BL21(DE3) as C-terminal SUMO fusions, and EGFR-ECD was expressed in *Sf9* cells. Both were purified by Ni-affinity chromatography followed by size-exclusion chromatography (SEC) (Fig. 4a–d). Binding was measured by SPR, with EGFR-ECD immobilised on the chip and each binder injected as the analyte (Fig. 5a–k). All eleven constructs bound, with apparent KD values ranging from 0.54 μM for Binder 5 to 11.5 μM for Binder 2 (Fig. 5l; Table 1). The best binder therefore reaches only submicromolar affinity (540 nM); no construct bound in the low-nanomolar range. Within this dataset, every design that met the AF3 ipTM threshold bound.

## Discussion

This study began with a practical question: given a chosen epitope on the EGFR ectodomain, what does a standard RFdiffusion pipeline actually deliver? Across eleven epitopes the answer was uneven. Designs passed the computational filters readily when aimed at DIII, rarely for the DI input, and not at all for the DII/DIII composite or the EGFRvIII-derived DIV surface. The eleven DIII-directed binders we carried to experiment all bound EGFR, but in the micromolar range. The most useful part of the result may be the negative one. Two of the eleven structures returned no design passing a filter that seven of the other nine satisfied thousands of times, and one further input returned only nine. For a laboratory deciding where to spend a design campaign, that contrast is actionable, and it is invisible in the aggregate success rates that are usually reported.

The outcome was set by the epitope rather than by the subdomain label. Hotspot number did not explain the twentyfold spread within DIII: the 4UV7 and 3C09 hotspot sets are similar in size but sit on different parts of the surface, 325–362 in the N-terminal half of DIII versus 449–466 close to the DIII–DIV junction, so the shape and continuity of the patch that a hotspot set defines is the more plausible cause. We therefore read the dominance of DIII as a property of the eleven epitopes examined rather than of the subdomain as such. Subdomain identity is confounded with epitope geometry and with target cropping, and most subdomains are represented here by only one or a few structures. The practical implication holds regardless of that ambiguity: before committing a campaign to one surface, survey several.

Two protocol-level observations follow from the same dataset. Binder length mattered: the 50–59 residue class gave the highest pass rate, designs of 40–69 residues accounted for 60% of all passing designs, and the rate halved by 90–99 residues. This agrees with the shorter-is-better trend reported for BindCraft[19], although the pooled optimum was target-dependent, so it is a tendency to weight in planning rather than a rule to design by. A single FastRelax cycle raised the pass rate only marginally and barely changed the score distribution; the step is helpful but not essential in this setting, which matches the observation of the RFdiffusion authors that relaxation did not produce large gains *in silico*[12].

AF2 and AF3 confidence scores answer a different question from the one an experimentalist asks. All eleven binders scored an ipTM between 0.90 and 0.94 — a range truncated by the selection threshold and far too narrow to rank them — while their affinities spanned more than twentyfold: the design with the highest ipTM (Binder 7, 0.94) bound eight times more weakly than Binder 5, one of the four designs sharing the lowest ipTM (0.90). The same mismatch has been documented at scale in the Adaptyv EGFR competition, where 601 designs were expressed and measured and the metrics in common use ranked them poorly against experiment[21]. The reason is straightforward. AF2 and AF3 predict whether a complex is structurally plausible; they do not score the packing, desolvation and electrostatics that set affinity, so a filter selecting for a well-formed interface admits designs of very different quality. Within this dataset the ipTM threshold did work as a binary indicator — every design with an ipTM of 0.9 or higher that we took to experiment bound — but it carried no information about how strongly.

The micromolar affinities should be read against what the pipeline was asked to do. It selected designs in a single computational pass, with no experimental screening and no interface optimisation, whereas the earlier EGFR campaigns that reached nanomolar affinity combined design with exactly those steps[10,20]; the best design in the Adaptyv competition, 82 nM, emerged from the same kind of iteration[21]. Closing the remaining gap to nanomolar affinity is therefore a matter of iterative refinement after the first pass, not of a different design pipeline.

The comparison has clear limits. It covers one receptor, one pipeline, one set of filters and one experimental readout; most subdomains are represented by a single structure, and the epitope-level differences we emphasise cannot be cleanly separated from cropping and structure-specific effects. Whether DIII is intrinsically more designable, or simply better sampled in our panel, can only be settled with more inputs per subdomain and, eventually, experimental tests beyond the eleven binders reported here. The broader lesson does not depend on that answer. The yield of a de novo binder campaign is set largely by the surface that is chosen, so epitopes should be surveyed before commitment, confidence metrics should be treated as binary filters rather than affinity predictors, and the budget should allow for affinity maturation after the first computational pass.

# Methods

***Binder scaffold design with RFdiffusion***

Eleven EGFR–antagonist complexes were selected. For each, the EGFR chain was cropped to a segment that encompasses the interface and was used as the design target; the following residue ranges were used: 308–502 on chain M of PDB 3B2U; 310–501 on chain M of 5SX5; 310–500 on chain A of 3C09; 310–503 on chain A of 3P0Y; 310–502 on chain A of 4UV7; 310–502 on chain A of 5XWD; 307–502 on chain K of 4KRM; 208–612 on chain A of 4KRP; 303–612 on chain B of 8UKV; 310–613 on chain A of 4UIP; and 2–209 on chain A of 3QWQ. Residue numbering follows the deposited construct for each structure. Hotspots were identified using the *interfaces* tool in ChimeraX[32]. 8UKV is an EGFRvIII-derived construct and was used as deposited.

For each target, six design jobs were performed with binder lengths of 40–49, 50–59, 60–69, 70–79, 80–89 and 90–99 amino acids, each generating 1,000 backbones. The Complex_beta_ckpt.pt weights were used rather than the default model, because the default checkpoints are strongly enriched in α-helical folds and the β-sheet-biased checkpoint broadens the topology of the starting scaffolds[12]; denoiser parameters were noise_scale_ca = 0.5 and noise_scale_frame = 0.5. In total, 6,000 backbones were generated per target and 66,000 across the eleven targets.

***Binder sequence design with ProteinMPNN***

Scaffold PDB files generated by RFdiffusion (v1.1.0) were converted to silent format using Rosetta SilentFile utilities. Sequence assignment was carried out with ProteinMPNN[15] through the dl_binder_design package (v1.0.0) with default parameters. Five sequences were requested per backbone: four from the unrelaxed output and a fifth after one cycle of FastRelax[31]. This yielded 30,000 sequences per target and 330,000 in total.

***Binder structure prediction and filtering with AlphaFold2***

Binder structures were predicted with AF2 as implemented in dl_binder_design[10] using the initial-guess protocol. Designs were filtered on PAE_interaction < 10, binder pLDDT > 80 and binder Cα RMSD < 1 Å, where pLDDT is that of the binder chain, RMSD is measured after superposition of the predicted binder on the design model, and PAE_interaction is the mean predicted aligned error over the interchain residue pairs at the predicted interface. Designs with PAE_interaction < 5 were evaluated on the AlphaFold3 server[33], and those with ipTM ≥ 0.90 were then inspected manually before the final selection.

### *Binder expression and purification*

Constructs comprised, from the N- to the C-terminus, the binder sequence, the SNAC cleavage motif (GSHHW)[34], a SUMO tag and a hexahistidine tag; where a design lacked an initiating methionine, an MSG tripeptide was appended at the N-terminus. The fusion adds approximately 13 kDa to the binder, giving calculated masses of 21–24 kDa for the eleven constructs (binders alone, 7.7–11.1 kDa). Codon-optimised genes were synthesised and inserted into pET21b via *Nde*I and *Bam*HI sites (Suzhou Genewiz Biotechnology Co., Ltd.). Recombinant proteins were expressed in *E. coli* BL21(DE3) in Terrific Broth containing 50 µg/mL ampicillin. Expression was induced with 0.5 mM IPTG at an $OD_{600}$ of 1.0, followed by incubation at 16 °C overnight.

For purification, cell pellets were resuspended in lysis buffer (20 mM HEPES-Na, pH 8.0, 300 mM NaCl, 10 mM imidazole) and disrupted by high-pressure homogenisation. The lysate was clarified at 40,000 × g for 30 min and the supernatant loaded onto a Ni-NTA column. Bound protein was eluted stepwise in 20 mM HEPES-Na, pH 7.5, 150 mM NaCl, 10% glycerol with 20, 50 or 300 mM imidazole. The 300 mM fraction was concentrated in a 10-kDa cut-off device and polished by SEC on a Superdex 200 Increase 10/300 GL column (Cytiva) in 25 mM HEPES-Na, pH 7.5, 150 mM NaCl. The SUMO tag was retained throughout; no cleavage step was performed, and the eluted fusion proteins were used directly for SPR.

### *EGFR-ECD expression and purification*

EGFR-ECD proteins were expressed in Sf9 insect cells using the Bac-to-Bac baculovirus system. Cells at a density of 3.0 × $10^6$ cells/mL were infected and cultured at 27 °C for 60 h. The supernatant was harvested by centrifugation at 4,000 × g for 30 min and loaded onto a Ni-NTA column. Bound proteins were eluted stepwise with buffers containing 20 mM HEPES-Na pH 7.5, 150 mM NaCl, 10% glycerol, and imidazole at 20, 50 or 300 mM. The 300 mM imidazole fraction was collected, concentrated using a 50-kDa MWCO centrifugal device, and further purified by size-exclusion chromatography on a Superdex 200 Increase 10/300 GL column (Cytiva) equilibrated with 25 mM HEPES-Na pH 7.5 and 150 mM NaCl.

### *SPR assay*

SPR was performed on a Biacore 8K+ instrument (Cytiva, Massachusetts, USA). EGFR-ECD was immobilised on a CM5 sensor chip by standard amine coupling (NHS/EDC); a reference flow cell was activated and deactivated without protein, and all responses were referenced to it. Measurements were made at 25 °C. Each binder was injected as a twofold dilution series over the immobilised surface, with the range chosen for each binder according to its response and spanning 0.16–20 µM overall (Fig. 5). Each cycle comprised a 90-s association and a 90-s dissociation phase at a flow rate of 30 µL/min in running buffer (20 mM HEPES-Na, pH 7.5, 150 mM NaCl, 0.05% Tween-20). The surface was regenerated between cycles with 10 mM glycine-HCl, pH 2.0, for 30 s at 30 µL/min. Sensorgrams were fitted to a 1:1 Langmuir model in Biacore Insight Evaluation Software v5.0 (Cytiva). Final figures were prepared with GraphPad Prism v9.5.1 (Dotmatics, San Diego, CA, USA).

### *Use of large language models*

During preparation of this manuscript we used DeepSeek (accessed September 2026) to polish the language of our own draft: wording, grammar, punctuation and sentence-level readability, across the title, abstract, introduction, results, discussion and methods. The tool was not used to collect or analyse data, to generate figures, or to develop or interpret the scientific content, and it did not influence our conclusions. Every change was checked by the authors against the original text and, where a sentence carried a result or a citation, against the underlying data and the cited reference; suggestions that altered the intended meaning were rejected. Only our own draft text was entered into the tool. The authors reviewed and approved the final version and take full responsibility for its accuracy, integrity and originality.

## Declarations

# Competing interests

The authors declare no competing interests.

# Author Contribution

S.Z. and W.Z. contributed equally. S.Z.: investigation, validation, methodology, visualisation, writing—original draft, writing—review and editing. W.Z.: investigation, validation, writing—original draft, writing—review and editing. G.Z., Z.C., B.C. and Y.M.: writing—review and editing. H.J.: conceptualisation, funding acquisition, investigation, validation, visualisation, writing—original draft, writing—review and editing. H.H.: conceptualisation, funding acquisition, supervision, project administration, investigation, validation, visualisation, writing—original draft, writing—review and editing. J.X.: conceptualisation, funding acquisition, supervision, project administration, investigation, validation, visualisation, writing—original draft, writing—review and editing.

# Acknowledgement

This work was supported by the National Natural Science Foundation of China (grant numbers 52388101 to J.X., 32471254 and 82430027 to H.H., and 32501293 to H.J.), and the Shenzhen Science and Technology Innovation Committee (JCYJ20240813113600001 to H.H.). It was also supported by the Shenzhen Medical Research Fund (A2403008 to H.J.). The time of H.H. during this work was supported by the Kobilka Institute of Innovative Drug Discovery and Presidential Fellowship and University Development Fund at The Chinese University of Hong Kong, Shenzhen, and by the Guangdong Provincial Department of Science and Technology (2024TQ08A721 to H.H.). We thank Xuezhen Lin from the Sample Preparation and Analysis Core Facility of the Bio-Tech Center at the Shenzhen Medical Academy of Research and Translation (SMART) for performing the SPR analysis.

# Data Availability

The per-design sequences and AF2 scores for all 330,000 designs are provided as Supplementary Information, and the AF3 scores for the eleven expressed binders are given in Table 1.

## References

1. Yarden, Y. & Sliwkowski, M. X. Untangling the ErbB signalling network. *Nat. Rev. Mol. Cell. Biol.* **2**, 127–137 (2001).
2. Chen, J. C. et al. Expression and function of the epidermal growth factor receptor in physiology and disease. *Physiol. Rev.* **96**, 1025–1069 (2016).
3. Pan, P. C. & Magge, R. S. Mechanisms of EGFR resistance in glioblastoma. *Int. J. Mol. Sci.* **21**, 8471 (2020).
4. Wang, S. M. et al. PD-L2 drives resistance to EGFR-TKIs: dynamic changes of the tumor immune environment and targeted therapy. *Cell. Death Differ.* **31**, 1140–1156 (2024).
5. Li, S. et al. Structural basis for inhibition of the epidermal growth factor receptor by cetuximab. *Cancer Cell.* **7**, 301–311 (2005).
6. Sickmier, E. A. et al. The panitumumab EGFR complex reveals a binding mechanism that overcomes cetuximab induced resistance. *PLOS One*. **11**, e0163366 (2016).

7. Wurch, T. et al. Development of novel protein scaffolds as alternatives to whole antibodies for imaging and therapy: status on discovery research and clinical validation. *Curr. Pharm. Biotechnol.* **9**, 502–509 (2008).
8. Simeon, R. & Chen, Z. L. In vitro-engineered non-antibody protein therapeutics. *Protein Cell.* **9**, 3–14 (2018).
9. Luo, R. L., Liu, H. G. & Cheng, Z. Protein scaffolds: antibody alternatives for cancer diagnosis and therapy. *RSC Chem. Biol.* **3**, 830–847 (2022).
10. Cao, L. X. et al. Design of protein-binding proteins from the target structure alone. *Nature* **605**, 551–560 (2022).
11. Höcker, B. et al. How can the protein design community best support biologists who want to harness AI tools for protein structure prediction and design? *Cell. Syst.* **14**, 629–632 (2023).
12. Watson, J. L. et al. De novo design of protein structure and function with RFdiffusion. *Nature* **620**, 1089–1100 (2023).
13. Bennett, N. R. et al. Improving de novo protein binder design with deep learning. *Nat. Commun.* **14**, 2625 (2023).
14. Notin, P. et al. Machine learning for functional protein design. *Nat. Biotechnol.* **42**, 216–228 (2024).
15. Dauparas, J. et al. Robust deep learning-based protein sequence design using ProteinMPNN. *Science* **378**, 49–56 (2022).
16. Jumper, J. et al. Highly accurate protein structure prediction with AlphaFold. *Nature* **596**, 583–589 (2021).
17. Vázquez Torres, S. et al. De novo design of high-affinity binders of bioactive helical peptides. *Nature* **626**, 435–442 (2024).
18. Glögl, M. et al. Target-conditioned diffusion generates potent TNFR superfamily antagonists and agonists. *Science* **386**, 1154–1161 (2024).
19. Pacesa, M. et al. One-shot design of functional protein binders with BindCraft. *Nature* **646**, 483–492 (2025).
20. Xia, Z. et al. Targeting overexpressed antigens in glioblastoma via CAR T cells with computationally designed high-affinity protein binders. *Nat. Biomed. Eng.* **8**, 1634–1650 (2024).
21. Cotet, T. S. et al. Crowdsourced protein design: lessons from the Adaptyv EGFR binder competition. *bioRxiv* (2025). https://doi.org/10.1101/2025.04.17.648362
22. Li, S., Kussie, P. & Ferguson, K. M. Structural basis for EGF receptor inhibition by the therapeutic antibody IMC-11F8. *Structure* **16**, 216–227 (2008).
23. Schmiedel, J., Blaukat, A., Li, S., Knöchel, T. & Ferguson, K. M. Matuzumab binding to EGFR prevents the conformational rearrangement required for dimerization. *Cancer Cell.* **13**, 365–373 (2008).
24. Schaefer, G. et al. A two-in-one antibody against HER3 and EGFR has superior inhibitory activity compared with monospecific antibodies. *Cancer Cell.* **20**, 472–486 (2011).
25. Lim, Y. et al. GC1118, an anti-EGFR antibody with a distinct binding epitope and superior inhibitory activity against high-affinity EGFR ligands. *Mol. Cancer Ther.* **15**, 251–263 (2016).
26. Matsuda, T. et al. Cell-free synthesis of functional antibody fragments to provide a structural basis for antibody-antigen interaction. *PLOS One*. **13**, e0193158 (2018).
27. Schmitz, K. R., Bagchi, A., Roovers, R. C., van Bergen, P. M. P. & Ferguson, K. M. Structural evaluation of EGFR inhibition mechanisms for nanobodies/VHH domains. *Structure* **21**, 1214–1224 (2013).
28. Lee, J. J. et al. Enzymatic prenylation and oxime ligation for the synthesis of stable and homogeneous protein-drug conjugates for targeted therapy. *Angew Chem.* **54**, 12020–12024 (2015).
29. Ramamurthy, V. et al. Structures of adnectin/protein complexes reveal an expanded binding footprint. *Structure* **20**, 259–269 (2012).
30. Bagchi, A. et al. Structural insights into the role and targeting of EGFRvIII. *Structure* **32**, 1367–1380e6 (2024).

31. Conway, P., Tyka, M. D., DiMaio, F., Konerding, D. E. & Baker, D. Relaxation of backbone bond geometry improves protein energy landscape modeling. *Protein Sci.* **23**, 47–55 (2014).
32. Pettersen, E. F. et al. UCSF ChimeraX: structure visualization for researchers, educators, and developers. *Protein Sci.* **30**, 70–82 (2021).
33. Abramson, J. et al. Accurate structure prediction of biomolecular interactions with AlphaFold 3. *Nature* **630**, 493–500 (2024).
34. Dang, B. et al. SNAC-tag for sequence specific chemical protein cleavage. *Nat. Methods*. **16**, 319–322 (2019).

# Table

**Table 1. Designs selected for experimental testing.**

PAE_int, PAE_interaction; pLDDT and RMSD refer to the binder chain (see Methods). ipTM is from the AlphaFold3 server. $K_D$ values are apparent affinities of the SUMO-fusion constructs, fitted with a 1:1 model.

| Binder | Design ID | Length (aa) | FastRelax | PAE_int (Å) | pLDDT | RMSD (Å) | AF3 ipTM | KD (μM) |
|---|---|---|---|---|---|---|---|---|
| 1 | 3B2U_090_421_dldesign_3 | 93 | no | 4.628 | 90.9 | 0.99 | 0.93 | 5.60 |
| 2 | 5SX5_080_477_dldesign_0 | 85 | no | 4.279 | 94.1 | 0.55 | 0.92 | 11.5 |
| 3 | 5SX5_090_635_dldesign_2 | 98 | no | 4.583 | 92.8 | 0.56 | 0.90 | 2.59 |
| 4 | 3P0Y_070_795_dldesign_0_cycle1 | 70 | yes | 4.589 | 92.7 | 0.56 | 0.92 | 3.23 |
| 5 | 3P0Y_070_980_dldesign_0_cycle1 | 76 | yes | 4.954 | 91.8 | 0.97 | 0.90 | 0.54 |
| 6 | 3P0Y_080_52_dldesign_0_cycle1 | 81 | yes | 4.666 | 92.4 | 0.71 | 0.93 | 6.98 |
| 7 | 4UV7_070_221_dldesign_0_cycle1 | 72 | yes | 4.310 | 91.8 | 0.56 | 0.94 | 4.51 |
| 8 | 4UV7_090_376_dldesign_1 | 94 | no | 4.869 | 91.9 | 0.44 | 0.90 | 0.87 |
| 9 | 5XWD_080_527_dldesign_0_cycle1 | 87 | yes | 4.941 | 91.4 | 0.75 | 0.91 | 10.7 |
| 10 | 5XWD_090_878_dldesign_0 | 91 | no | 4.757 | 93.0 | 0.48 | 0.92 | 3.58 |
| 11 | 4KRM_070_638_dldesign_2 | 78 | no | 4.816 | 90.0 | 0.74 | 0.90 | 8.33 |

# Figures

**a**

| PDB | complexed with | target | hotspots | subdomain |
|---|---|---|---|---|
| 3B2U | Fab IMC-11F8 | M308-502 | 349,384,409,412,417,418,438,440,443,465,467,468,473 | DIII |
| 5SX5 | panitumumab | M310-501 | 349,353,384,409,417,418,438,443,465,467,468 | DIII |
| 3C09 | matuzumab | A310-500 | 449,452,454,455,457,458,459,460,463,464,466 | DIII |
| 3P0Y | Fab DL11 | A310-503 | 409,411,412,417,436,438,454,460,461,463,464,465,467 | DIII |
| 4UV7 | Fab GC1118A | A310-502 | 325,350,353,355,356,357,359,361,362 | DIII |
| 5XWD | 059-152-Fv | A310-502 | 322,323,325,346,349,350,353,355,357,382,384,408,409,417,418,438,440,441,443,465,467,468 | DIII |
| 4KRM | nanobody 7D12 | K307-502 | 325,348,349,350,353,355,357,384,409,418,468 | DIII |
| 4KRP | nanobody 9G8 | A208-612 | 292,293,306,310,375,376,400,401,403,405,430,431,433,455,457,458,460 | DII, DIII |
| 8UKV | nanobody 34E5 | B303-612 | 527,539,554,556,558,559,562,564,565,566,585,590,591,592,594,595 | DIV |
| 4UIP | repebody rAC1 | A310-613 | 411,417,438,440,441,449,450,452,454,463,464,465,467,468,469,471,472,473,476,488 | DIII, DIII-DIV linker |
| 3QWQ | adnectin | A2-209 | 12,14,15,16,17,18,45,69,99,101,103,125,128 | DI |

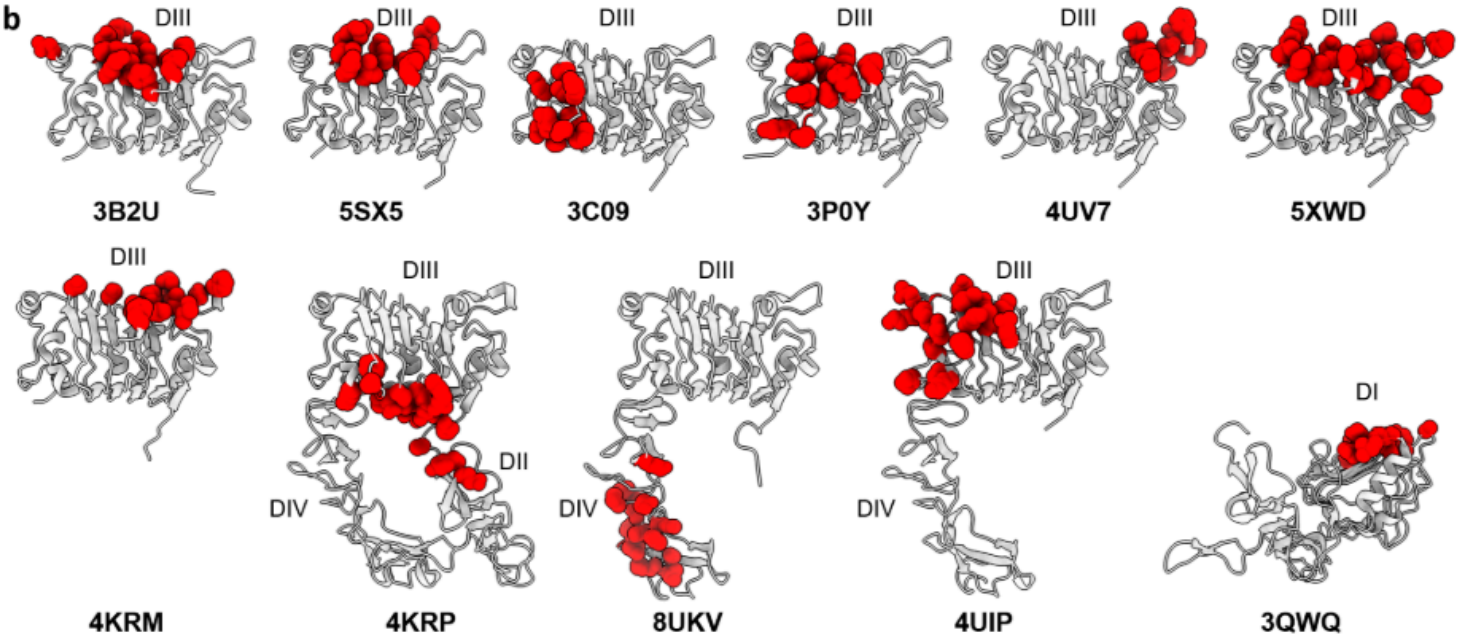


**Figure 1**

Target and hotspot selection for designing protein binders against the EGFR extracellular domain.

(a) Crystal structures used for binder design. For each PDB entry the table lists the bound antagonist, the cropped target region (chain and residue numbers) and the hotspot residues used in RFdiffusion. (b) Hotspot residues (red spheres) mapped onto the selected target structures (grey cartoon). The eleven inputs are grouped by the subdomain from which the hotspots derive: DIII only (3B2U, 5SX5, 3C09, 3P0Y, 4UV7, 5XWD, 4KRM), DII/DIII composite (4KRP), DIV (8UKV), DIII plus the DIII–DIV linker (4UIP) and DI (3QWQ).

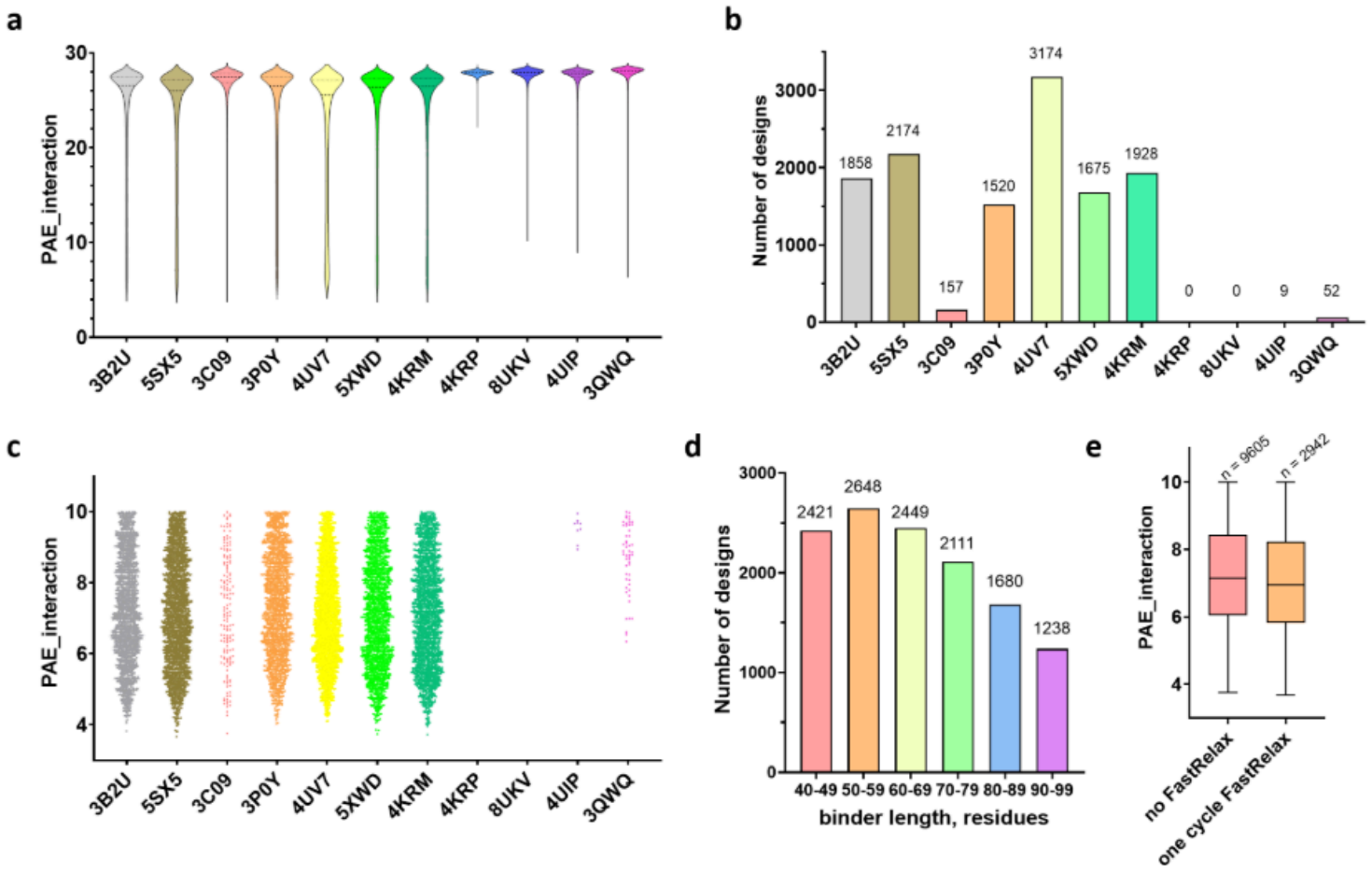


**Figure 2**

Statistics of the designed protein binders.

(a) Distribution of PAE_interaction values for all designs generated by RFdiffusion; data are presented as violin plot. (b) Number of designs passing the filter (PAE_interaction < 10, pLDDT > 80, RMSD < 1 Å). (c) Distribution of PAE_interaction values for designs that passed the filter; data are presented as violin plot with points. Medians of passing designs: 3B2U 7.098, 5SX5 7.061, 3C09 7.123, 3P0Y 7.333, 4UV7 7.020, 5XWD 7.096, 4KRM 7.117, 4UIP 9.663 and 3QWQ 8.834; 4KRP and 8UKV yielded no passing designs. (d) Number of passing designs by binder length class (residues); each class was generated from 55,000 sequences. (e) Distribution of PAE_interaction for passing designs generated without FastRelax and with one cycle; data are presented as median with interquartile range; box = 25th–75th percentile, line = median, whiskers = min to max. Median PAE_interaction is 7.154 Å without FastRelax and 6.955 Å with one cycle.

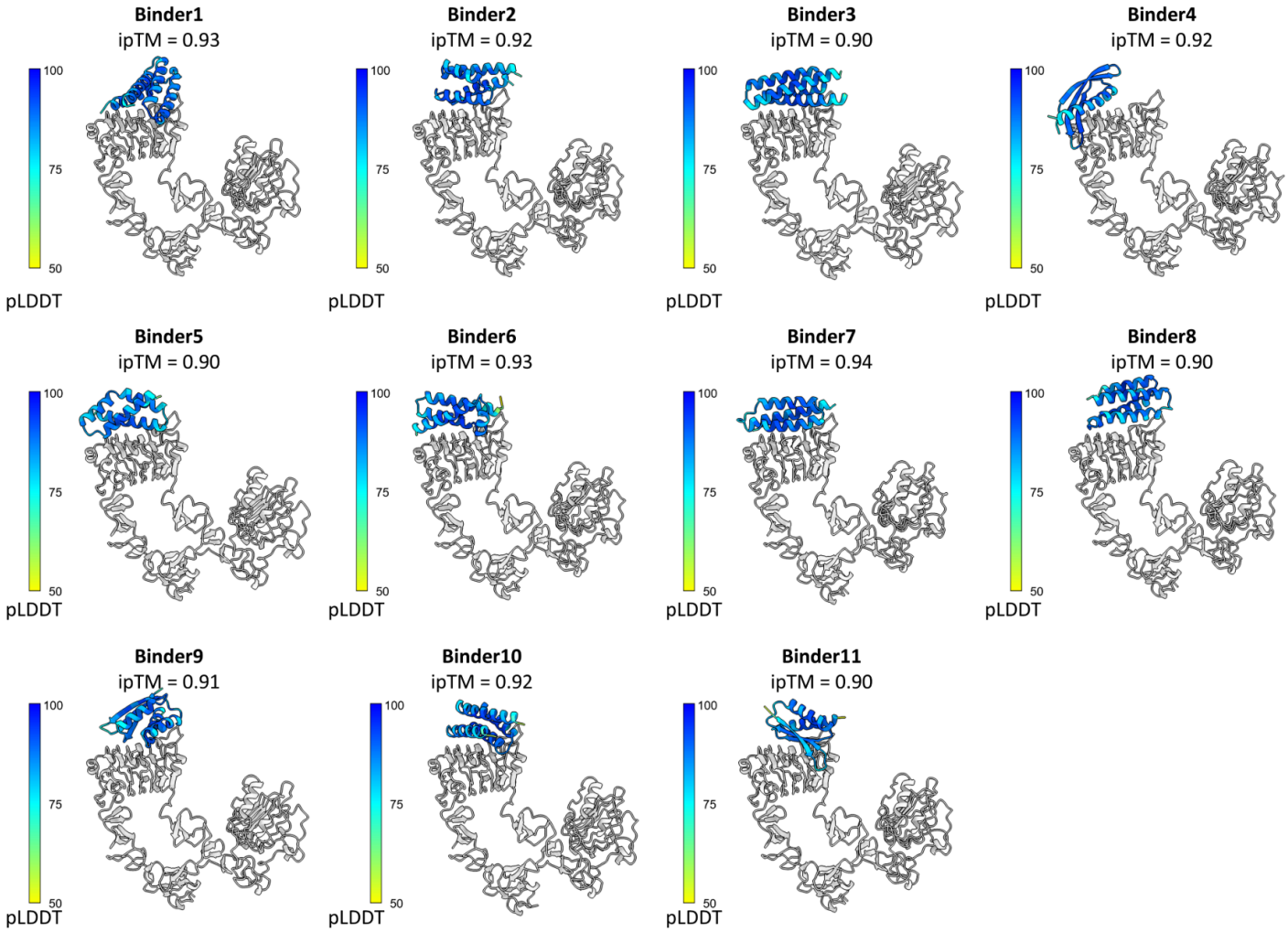


**Figure 3**

Binders selected for expression and purification.

AlphaFold3-predicted structures of the selected binders (cartoon, coloured by pLDDT) in complex with EGFR-ECD (cartoon, grey).

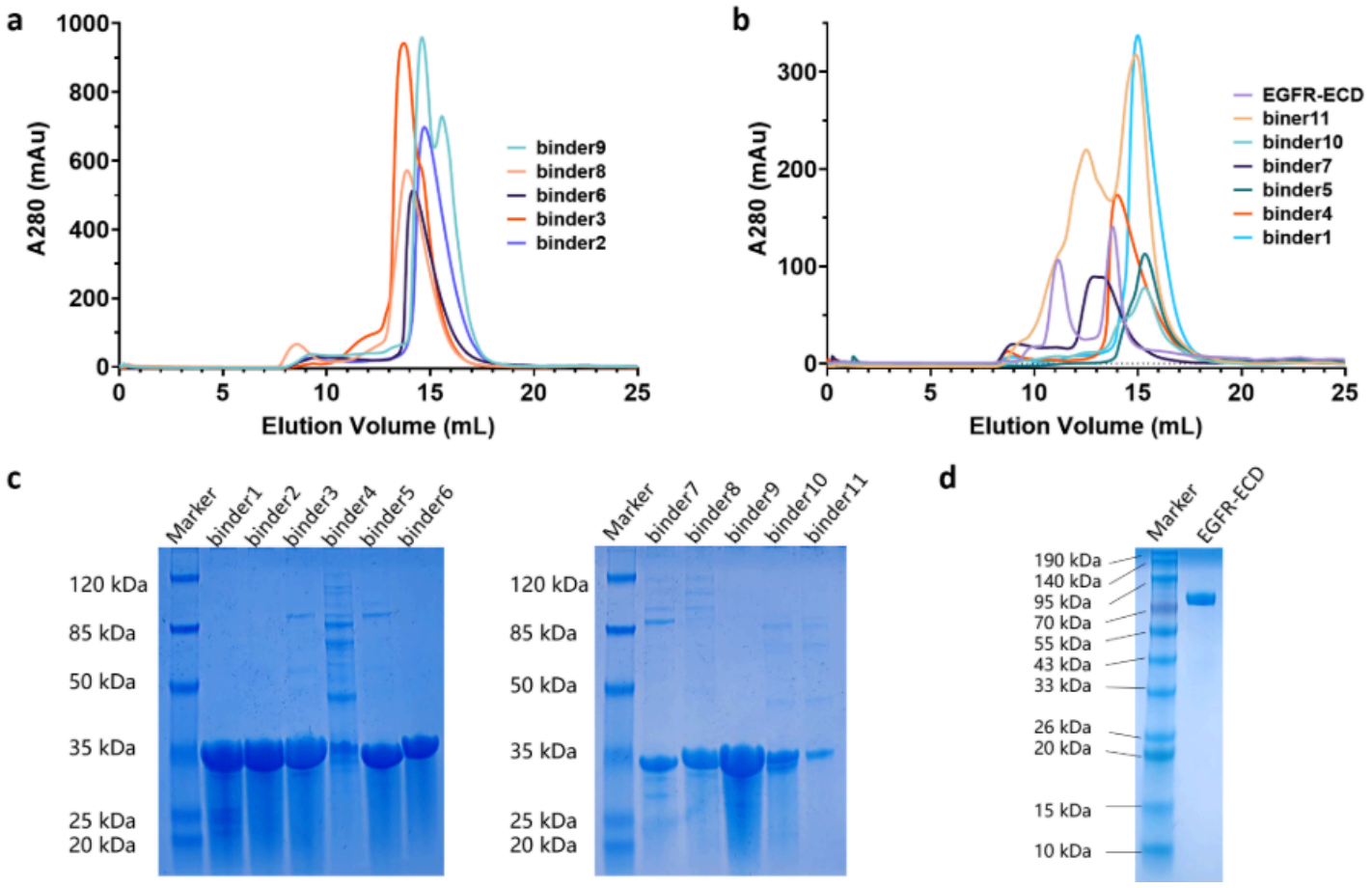


**Figure 4**

Purification of the designed protein binders.

(a,b) Size-exclusion chromatography profiles of Binders 1–11 and of the EGFR extracellular domain. (c) SDS–PAGE of the purified binders. (d) SDS–PAGE of purified EGFR-ECD. The corresponding uncropped SDS–PAGE gel images are provided in Supplementary Fig. S3.

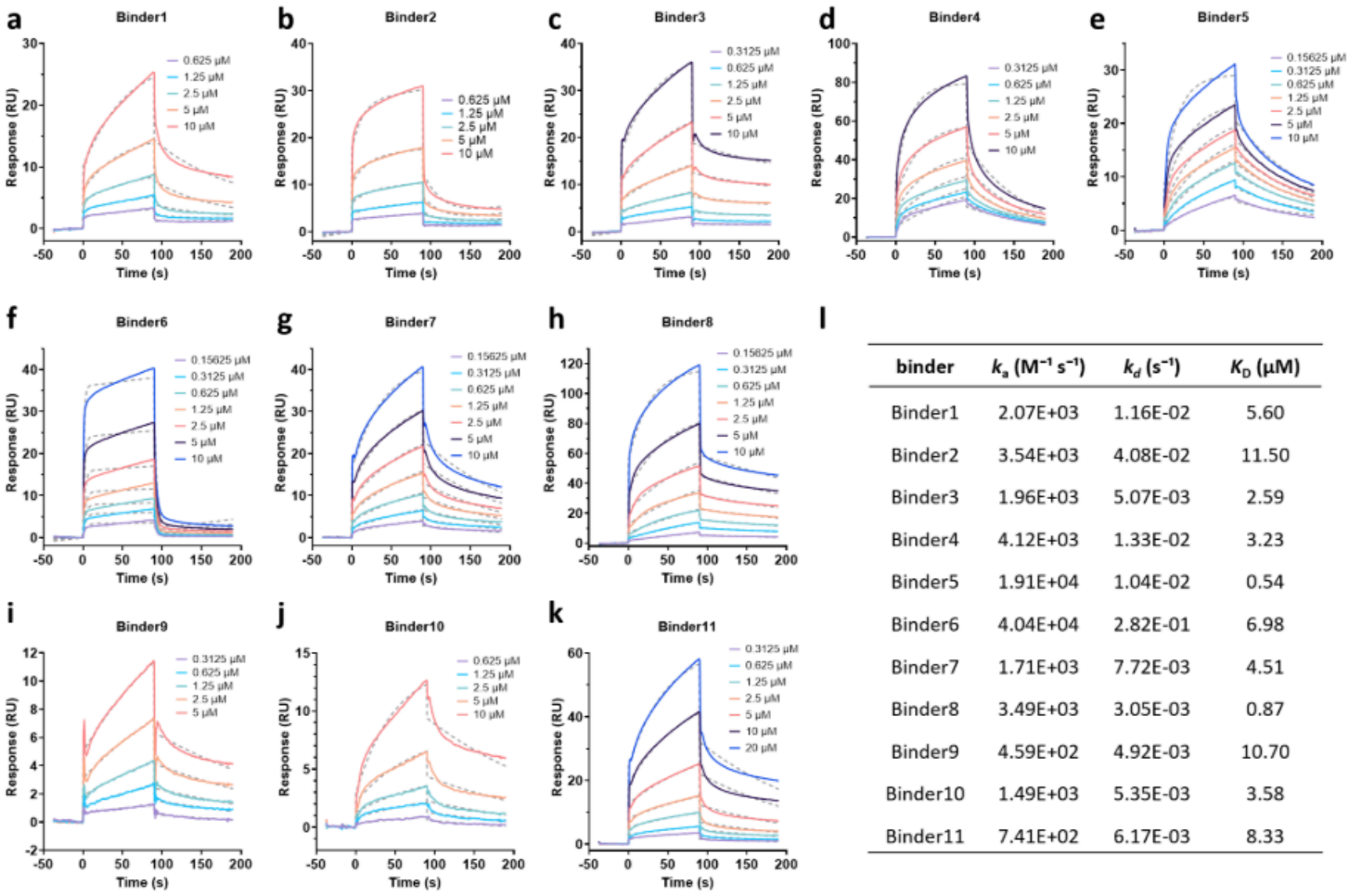


l

| binder | $k_a$ ($M^{-1}$ $s^{-1}$) | $k_d$ ($s^{-1}$) | $K_D$ (μM) |
|---|---|---|---|
| Binder1 | 2.07E+03 | 1.16E-02 | 5.60 |
| Binder2 | 3.54E+03 | 4.08E-02 | 11.50 |
| Binder3 | 1.96E+03 | 5.07E-03 | 2.59 |
| Binder4 | 4.12E+03 | 1.33E-02 | 3.23 |
| Binder5 | 1.91E+04 | 1.04E-02 | 0.54 |
| Binder6 | 4.04E+04 | 2.82E-01 | 6.98 |
| Binder7 | 1.71E+03 | 7.72E-03 | 4.51 |
| Binder8 | 3.49E+03 | 3.05E-03 | 0.87 |
| Binder9 | 4.59E+02 | 4.92E-03 | 10.70 |
| Binder10 | 1.49E+03 | 5.35E-03 | 3.58 |
| Binder11 | 7.41E+02 | 6.17E-03 | 8.33 |

**Figure 5**

Binding kinetics of the purified binders.

(a–k) SPR sensorgrams for Binders 1–11; the analyte concentration series is indicated in each panel and spans 0.16–20 μM overall. (l) Association ($k_a$) and dissociation ($k_d$) rate constants and dissociation constants ($K_D$) from a 1:1 Langmuir fit.

## Supplementary Files

This is a list of supplementary files associated with this preprint. Click to download.

- SupplementaryInformation.docx
- 20261112SupportingInformationfile.xlsx